

Alma Mater Studiorum Università di Bologna
Archivio istituzionale della ricerca

Time-Resolved Optical Pump-Resonant X-ray Probe Spectroscopy of 4-Thiouracil: A Simulation Study

This is the final peer-reviewed author's accepted manuscript (postprint) of the following publication:

Published Version:

Nam, Y., Montorsi, F., Keefer, D., Cavaletto, S.M., Lee, J.Y., Nenov, A., et al. (2022). Time-Resolved Optical Pump-Resonant X-ray Probe Spectroscopy of 4-Thiouracil: A Simulation Study. JOURNAL OF CHEMICAL THEORY AND COMPUTATION, 18(5), 3075-3088 [10.1021/acs.jctc.2c00064].

Availability:

This version is available at: <https://hdl.handle.net/11585/899348> since: 2023-05-12

Published:

DOI: <http://doi.org/10.1021/acs.jctc.2c00064>

Terms of use:

Some rights reserved. The terms and conditions for the reuse of this version of the manuscript are specified in the publishing policy. For all terms of use and more information see the publisher's website.

This item was downloaded from IRIS Università di Bologna (<https://cris.unibo.it/>).
When citing, please refer to the published version.

(Article begins on next page)

This is the final peer-reviewed accepted manuscript of:

Time-Resolved Optical Pump-Resonant X-ray Probe Spectroscopy of 4-Thiouracil: A Simulation Study

Nam Y.;Montorsi F.;Keefer D.;Cavaletto S. M.;Lee J. Y.;Nenov A.;Garavelli M.;Mukamel S.

J. Chem. Theory Comput. 2022, 18, 3075–3088

The final published version is available online at:
<https://dx.doi.org/10.1021/acs.jctc.2c00064>

Terms of use:

Some rights reserved. The terms and conditions for the reuse of this version of the manuscript are specified in the publishing policy. For all terms of use and more information see the publisher's website.

This item was downloaded from IRIS Università di Bologna (<https://cris.unibo.it/>)

When citing, please refer to the published version.

Time-Resolved Optical-Pump, Resonant X-ray Probe Spectroscopy of 4-Thiouracil; a Simulation Study

Yeonsig Nam,^{*,†,‡,||} Francesco Montorsi,^{¶,||} Daniel Keefer,[†] Stefano M.
Cavaletto,[†] Jin Yong Lee,^{*,†,§} Artur Nenov,^{*,¶} Marco Garavelli,[¶] and Shaul
Mukamel^{*,†}

[†]*Department of Chemistry, University of California, Irvine, California 92697-2025, United
States*

[‡]*Convergence Research Center for Energy and Environmental Sciences, Sungkyunkwan
University, Suwon 16419, Korea*

[¶]*Dipartimento di Chimica Industriale “Toso Montanari,” Università degli Studi di
Bologna, I-40136 Bologna, Italy*

[§]*Department of Chemistry, Sungkyunkwan University, Suwon 16419, Korea*

^{||}*These authors contribute equally to this work.*

E-mail: yeonsign@uci.edu; jinylee@skku.edu; artur.nenov@unibo.it; smukamel@uci.edu

Abstract

We theoretically monitor the photoinduced $\pi\pi^* \rightarrow n\pi^*$ internal conversion process in 4-thiouracil (4TU), triggered by an optical pump. The element-sensitive spectroscopic signatures are recorded by a resonant X-ray probe tuned to the sulfur, oxygen, or the nitrogen K-edge. We employ high-level electronic structure methods optimized for core-excited electronic structure calculation combined with quantum nuclear

wavepacket dynamics computed on a two relevant nuclear modes, fully accounting for their quantum nature of nuclear motions. We critically discuss the capabilities and limitations of the resonant technique. For sulfur and nitrogen, we document a pre-edge spectral window free from ground state background and rich with $\pi\pi^*$ and $n\pi^*$ absorption features. The lowest sulfur K-edge shows strong absorption for both $\pi\pi^*$ and $n\pi^*$. In the lowest nitrogen K-edge window, we resolve a state-specific fingerprint of the $\pi\pi^*$ and an approximate timing of the conical intersection via its depletion. A spectral signature of the $n\pi^*$ transition, not accessible by UV/Vis spectroscopy, is identified. The oxygen K-edge is not sensitive to molecular deformations and gives steady transient absorption features without spectral dynamics. The $\pi\pi^*/n\pi^*$ coherence information is masked by more intense contributions from populations. Altogether, element-specific time-resolved resonant X-ray spectroscopy provides a detailed picture of the electronic excited-state dynamics and therefore a sensitive window into the photophysics of thiobases.

Introduction

Pump-probe spectroscopy is the simplest nonlinear optical technique for monitoring the photoinduced excited state dynamics in molecules.^{1,2} It has been used with immense success to resolve ultrafast internal conversion (IC) and inter-system crossing (ISC) in pyrimidine nucleobases³⁻⁶ and their thionated counterparts⁷⁻¹⁰ by probing in the visible (Vis) and ultraviolet (UV) regime. In thio-nucleobases, one or more carbonyl oxygen atoms are substituted with sulfur atoms which strongly affects their photophysics. Thiouracils (Scheme 1a), i.e. the thionated form of the uracil nucleobase, undergo internal conversion (IC) from an optically bright $\pi\pi^*$ state to a dark $n\pi^*$ state mediated by a conical intersection (CoIn). The IC is followed by an ISC to form a long-lived triplet state with high quantum yield which facilitates applications as site-specific photoprobe for photodynamic therapy,^{11,12} and as photoinduced crosslinkers.^{13,14} The intermediate dark $n\pi^*$ state of thiouracils has not been directly probed

so far by UV/Vis transient spectroscopy due to the low oscillator strength of its photoinduced absorption and emission.

X-ray free-electron lasers (XFELs) light sources provide intense pulses at frequencies ranging from the XUV to the hard-X-ray regime¹⁵ with high temporal, spectral, and spatial resolutions. XFEL-based probes, such as transient X-ray absorption (TRXAS) and photoelectron (TRXPS) spectroscopy,^{16–18} have been employed to monitor an electrocyclic ring-opening reaction,¹⁹ intersystem-crossing,²⁰ and the free evolution of molecules passing through CoIns^{21,22} with sub-10 fs temporal resolution.²³ The unique capability of TRXAS to resolve transiently populated dark states has been demonstrated for the nucleobases uracil²⁴ and thymine²⁵

Earlier we had proposed two off-resonant techniques for probing the passage through CoIns, namely transient redistribution of ultrafast electronic coherences in attosecond Raman signals (TRUECARS) and time-resolved X-ray diffraction (TRXD), and employed to study the IC in 4-thiouracil (4TU).²⁶ TRUECARS keeps track of vibronic coherences, thereby providing the temporal and spectral profiles of the CoIn in a background-free manner. TRXD images the time-evolving electron charge densities, hence provide real-space images of charge densities at CoIns. These off-resonant techniques can be used universally to obtain snapshots of the passage through the CoIn but do not carry information about the population evolution on the individual electronic states.

Here, we further address the $\pi\pi^* \rightarrow n\pi^*$ IC in 4TU and present an ab-initio computational protocol for obtaining element-sensitive core-to-valence spectroscopic signatures accessible through TRXAS using probe pulses resonant with either the sulfur, oxygen or nitrogen K-edges. To this aim, we employ multiconfigurational wave function-based electronic structure methods optimized for core-excited electronic structure calculations combined with grid-based exact quantum dynamics in reduced coordinate space. The capabilities and limitations of the resonant technique are discussed. Specifically, for sulfur and nitrogen we identify a pre-edge spectral window free from ground state absorption background and rich

with excited state absorption features. In the nitrogen pre-edge window we resolve clear $n\pi^*$ signatures which rise with a delay matching the $\pi\pi^*$ lifetime. We demonstrate that coherences created during the CoIn passage remain hidden under the more intense contributions from populations, making TRXAS complementary to the TRUECARS technique, which is insensitive to population dynamics.

Computational Protocol

Optical Pump - Resonant X-ray Probe signals

A UV/Vis pump brings the system into an optically bright valence excited state, or into a superposition thereof. A weak X-ray pulse then probes the nonadiabatic dynamics (Scheme 1a) at time delay T . The light-matter interactions and the evolution of the system can be represented diagrammatically by a loop diagram (Scheme 1b). The shaded area in the diagram represents an arbitrary excitation, which is then followed by the nonadiabatic dynamics (wavy lines). The left branch of the loop represents the time evolution of the ket wavepacket until the expectation value is taken at time t , whereas the right branch represents the time evolution of the bra wavepacket. After the interaction with the pump, the ket evolves in the valence manifold $|e\rangle$ according to the propagator $G_0(t - t_1)$. At time $t - t_1$, an incoming X-ray pulse (\mathcal{E}_{pr}) brings the molecule once again into the core-excited manifold $|f\rangle$. The core state has a very short lifetime, we thus neglect the nuclear dynamics during time t_1 and the propagation is represented by a solid line. The second interaction with the probe ($\mathcal{E}_{\text{pr}}^*$) at time t brings down the wavepacket into the valence state e' . The signal is finally calculated as the scalar product of the propagated ket and bra at time t . No interaction with the X-ray fields takes place in the right branch and the bra evolves in the valence manifold from the initial time to t using the propagator $G_0^\dagger(t)$.

The X-ray probe-matter interaction Hamiltonian in the rotating-wave approximation is

given by

$$H_{\text{int}} = -\mathbf{E}(t) \cdot \boldsymbol{\mu}^\dagger - \mathbf{E}^*(t) \cdot \boldsymbol{\mu}. \quad (1)$$

The dipole moment operator reads

$$\boldsymbol{\mu} = \sum_{ef} \boldsymbol{\mu}_{ef} |\phi_e\rangle \langle \phi_f| \quad (2)$$

where $\boldsymbol{\mu}_{ef}$ is a lowering operator acting on the nuclear space, with index e running over the valence excited states and the ground state and f running over the core-excited states of the molecule. The complex probe electric field centered at time T

$$\mathbf{E}(t) = \mathbf{e} \mathcal{E}(t - T) e^{-i\omega_0(t-T)} \quad (3)$$

has polarization vector \mathbf{e} , envelope $\mathcal{E}(t)$, and central frequency ω_0 . We introduce the Fourier transform

$$\mathbf{E}(\omega) = \mathbf{e} \mathcal{E}(\omega - \omega_0) e^{i\omega T} \quad (4)$$

The pump-probe signal is defined as the change in the frequency-dispersed transmitted probe pulse, i.e., the time-integrated rate of change of the number of photons at the probe signal frequency ω_s ,

$$S(\omega_s, T) = \int \left\langle \frac{dN(\omega_s)}{dt} \right\rangle dt. \quad (5)$$

Here, $N(\omega_s) = a^\dagger(\omega_s) a(\omega_s)$ is the number operator of a photon at the detected frequency ω_s , with the associated Boson creation and annihilation operators, $a^\dagger(\omega_s)$ and $a(\omega_s)$, respectively. Solving the Heisenberg equation of motion for N leads to

$$S(\omega_s, T) = -2\text{Im} \left[\mathcal{E}^*(\omega_s - \omega_0) \int dt e^{i\omega_s(t-T)} \langle \boldsymbol{\mu}(t) \rangle \cdot \mathbf{e} \right] \quad (6)$$

Expanding the evolution of the dipole operator $\langle \boldsymbol{\mu}(t) \rangle$ to first order in \mathcal{E} gives:

$$S(\omega_s, T) = -2\text{Im} \left[\mathcal{E}^*(\omega_s - \omega_0) \int dt \int_0^\infty dt_1 \mathcal{E}(t - t_1 - T) e^{i(\omega_s - \omega_0)(t - t_1 - T)} e^{i\omega_s t_1} \right. \\ \left. \times i \langle \Psi(t) | \boldsymbol{\mu} \cdot \mathbf{e} G_0(t, t - t_1) \boldsymbol{\mu}^\dagger \cdot \mathbf{e} | \Psi(t - t_1) \rangle \right]. \quad (7)$$

Here, $|\Psi(t)\rangle$ represents the free evolution of the system following the pump pulse. This is expanded in the basis $|\phi_e\rangle$ of adiabatic electronic states,

$$|\Psi(t)\rangle = \sum_e c_e(t) |\chi_e(t)\rangle |\phi_e\rangle \quad (8)$$

where $|\chi_e(t)\rangle$ is the time-dependent normalized nuclear wave packet on the e th valence-state potential energy surface and $c_e(t)$ is the amplitude of the e th state. The operator

$$G_0(t, t - t_1) = \sum_f G_{0,ff}(t, t - t_1) |\phi_f\rangle \langle \phi_f| \quad (9)$$

represents the free evolution of the molecule after it has been excited to a core state f , where $G_{0,ff}(t, t - t_1)$ is an operator in the nuclear space. By expanding the signal in the basis of adiabatic electronic states, we obtain:

$$S(\omega_s, T) = -2\text{Im} \left[\mathcal{E}^*(\omega_s - \omega_0) \int dt \int_0^\infty dt_1 \mathcal{E}(t - t_1 - T) e^{i(\omega_s - \omega_0)(t - t_1 - T)} e^{i\omega_s t_1} i \sum_{ee'f} c_{e'}^*(t) c_e(t - t_1) \right. \\ \left. \times \langle \chi_{e'}(t) | \boldsymbol{\mu}_{e'f} \cdot \mathbf{e} G_{0,ff}(t, t - t_1) \boldsymbol{\mu}_{fe}^\dagger \cdot \mathbf{e} | \chi_e(t - t_1) \rangle \right] \quad (10)$$

Since the core state is short lived, we neglect the propagation of the nuclear WP on the core state potential energy surfaces and describes it as the electronic modulation in core state f during t_1 ,

$$G_{0,ff}(t, t - t_1) = e^{-i\omega_f t_1 - \Gamma_f t_1} \quad (11)$$

We have used the following lifetime broadenings 0.613 eV (S 1s-edge), 0.18 eV (O 1s-edge), and 0.132 eV (N 1s-edge).²⁷ The signal finally reads,

$$S(\omega_s, T) = 2\text{Re} \left[\mathcal{E}^*(\omega_s - \omega_0) \int dt \int_0^\infty dt_1 \mathcal{E}(t - t_1 - T) e^{i(\omega_s - \omega_0)(t-T)} e^{i(\omega_0 - \omega_f + i\Gamma_f)t_1} \right. \\ \left. \times \sum_{ee'f} c_{e'}^*(t) c_e(t - t_1) \langle \chi_{e'}(t) | \boldsymbol{\mu}_{e'f} \cdot \mathbf{e} \boldsymbol{\mu}_{fe}^\dagger \cdot \mathbf{e} | \chi_e(t - t_1) \rangle \right]. \quad (12)$$

The optical-pump - X-ray probe signal for a single broadband probe reads,

$$S(\omega_s, T) = 2\text{Re} \left[\mathcal{E}_{\text{pr}}^*(\omega_s - \omega_{\text{pr}}) \int dt \int_0^\infty dt_1 \mathcal{E}_{\text{pr}}(t - t_1 - T) e^{i(\omega_s - \omega_{\text{pr}})(t-T)} e^{i(\omega_{\text{pr}} - \omega_f + i\Gamma_f)t_1} \right. \\ \left. \times \sum_{ee'f} c_{e'}^*(t) c_e(t - t_1) \langle \chi_{e'}(t) | \boldsymbol{\mu}_{e'f} \cdot \mathbf{e} \boldsymbol{\mu}_{fe}^\dagger \cdot \mathbf{e} | \chi_e(t - t_1) \rangle \right] \quad (13)$$

Replacing the single broadband probe pulse with a broadband/narrowband hybrid pulse, $\mathcal{E}_B/\mathcal{E}_N$ gives,

$$S(\omega_s, T) = 2\text{Re} \left[\mathcal{E}_B^*(\omega_s - \omega_B) \int dt \int_0^\infty dt_1 \mathcal{E}_N(t - t_1 - T) e^{i(\omega_s - \omega_N)(t-T)} e^{i(\omega_N - \omega_f + i\Gamma_f)t_1} \right. \\ \left. \times \sum_{ee'f} c_{e'}^*(t) c_e(t - t_1) \langle \chi_{e'}(t) | \boldsymbol{\mu}_{e'f} \cdot \mathbf{e} \boldsymbol{\mu}_{fe}^\dagger \cdot \mathbf{e} | \chi_e(t - t_1) \rangle \right] \quad (14)$$

where ω_N is the central frequency of the narrowband field giving the resonance conditions: $\omega_N = \omega_f$.

The simulation of TRXAS signal with optical pump and resonant X-ray probe using eqs. 13 and 14 requires the following quantities:

- the electronic structure of the valence manifold $|e\rangle$ accessible by the optical pump pulse
- the evolution of the system in the valence manifold including phenomena such as IC or ISC
- the electronic structure of the core-excited manifold resonant with the X-ray probe

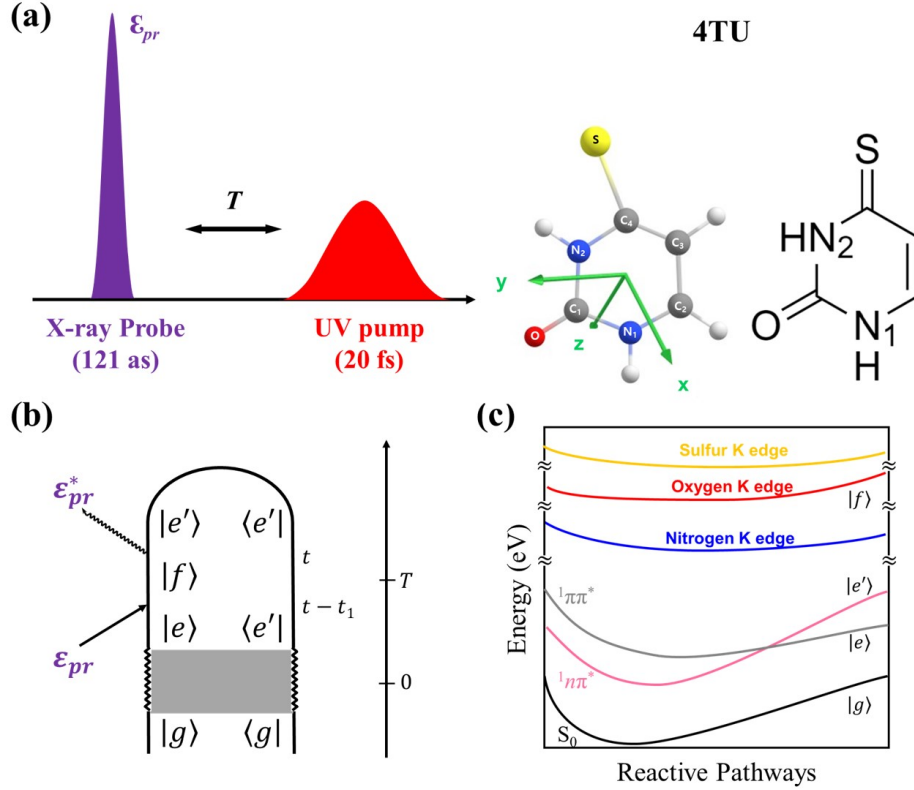
- the transition dipole moments between the valence and core-excited manifolds

In the following, we have performed pump-probe spectroscopy simulations to track the ultrafast $\pi\pi^* \rightarrow n\pi^*$ IC process in 4TU. The necessary ingredients are obtained at the ab initio level by combining state-of-the-art multiconfigurational wave function-based electronic structure calculations with grid-based exact quantum dynamics in reduced two-coordinate space.

Electronic structure calculations

The electronic structure of the valence manifold was obtained at the state-average complete active space self-consistent field (CASSCF) level followed by the single state (SS) flavor second order perturbation (CASPT2).²⁹ The active space consists of 12 electrons in 9 orbitals, comprising valence π -orbitals and the sulfur lone pair. Three states, the ground state, S_1 and S_2 , were included in the state averaging. In the CASPT2 routine, an imaginary shift of 0.2 was used³⁰ while the IPEA shift was set to 0.0.³¹ The ANO-L³² basis set was used with 5s4p2d1f contractions on sulfur, 4s3p2d1f on carbon, oxygen, nitrogen atoms, and 3s2p1d on hydrogen atoms. Stationary points on the S_2 and S_1 potential energy surfaces (PESs), i.e. the S_2 and S_1 minima and the S_2/S_1 CoIn, were optimized at the SS-CASPT2/SA-3-CASSCF(12,9) level using numerical energy gradients. The ground state minimum geometry was optimized at the MP2 level.

We have used a different active space and basis set for computing the spectroscopic signals (the calculation of valence-to-core states). In particular, we augment the 12,9 active space with three pairs of occupied (σ) / virtual (σ^*) orbitals and a single 1s core orbital for each heteroatom S, O, N₁ and N₂ (see scheme 1a for the labels). The additional $\sigma^{(*)}$ orbitals are required to converge the core-excited wavefunction and have a more complete set of spectral signatures in the regions of the PES where C–S and C–C bonds are significantly elongated. We employ the restricted active space formulation of the CASSCF method, known as RASSCF,³³ and place the 1s core orbital of a single heteroatom in RAS1, all occupied



Scheme 1: (a) Pulse configuration and molecular geometry of 4-thiouracil. The 20-fs FWHM Gaussian pump creates a population in the $S_2(\pi\pi^*)$ state. At time delay T , a single broadband X-ray probe pulse is used. (b) A Loop diagram for the optical pump - X-ray probe signal. The electronic excited state dynamics is monitored by the weak probe in the presence of a pump pulse initiating the evolution of a non-stationary state. An incoming X-ray pulse (\mathcal{E}_{pr}) excites a molecule on a ground/valence electronic surface $|e\rangle$ into a core level $|f\rangle$ after time delay T following an initial excitation into a non-stationary state and free evolution period (gray box). Then, signal field emission is stimulated by \mathcal{E}_{pr}^* . $e = e'$ gives excited absorption and ground state bleach signals while $e \neq e'$ gives a Raman signal. The complete diagram rules are given in Ref²⁸ and SI. (c) Energy level scheme of the measurement. Black, pink, and gray colors correspond to the ground state, $n\pi^*$, and $\pi\pi^*$ valence states and blue, red, and yellow colors correspond to nitrogen, oxygen, and sulfur K-edges, respectively.

orbitals in RAS2, and all virtual orbitals in RAS3, thereby allowing for one hole from RAS1 and up to four excitations into RAS3. We denote this active space as RAS(20,1,4;1,9,6) where the first three indices specify the number of electrons, the number of holes in RAS1, and of excitations in RAS3, respectively, while the last three denote the number of orbitals in the three sub-spaces.

Core-excited state calculations were performed within the core-valence separation (CVS)

framework through a projection technique known as HEXS (highly excited states)³⁴ which sets to zero CI coefficients of configuration state functions with maximum occupation from a given subspace, thus effectively projecting them out of the wavefunction. In particular, the lowest core-excited states for each heteroatom can be computed by applying the projection to the RAS1 subspace containing the 1s core orbital. Perturbation corrections were obtained with RASPT2,³⁵ i.e. second order perturbative correction on top of a RASSCF wavefunction, thereby using an imaginary value of 0.5 and setting the number of frozen orbitals to zero. Scalar relativistic effects were taken into account via a second order Douglas-Kroll-Hess Hamiltonian in combination with the ANO-RCC basis set^{36,37} with contractions 5s4p2d1f on sulfur, 4s3p2d1f on carbon, oxygen and nitrogen and 2s1p on hydrogen. At selected points initial tests with up to 30 core-excited states were performed that showed that a state-averaging of 10 states is sufficient in the case of oxygen and nitrogen to capture the dominant absorption signatures below the K-edge, whereas 30 states were averaged in the case of sulfur. A thorough benchmarking of the protocol has demonstrated a sub-eV accuracy of the predicted transition energies.³⁸ The valence states, ground state, S_1 , and S_2 , were recomputed with the same protocol, i.e. with the 1s core orbital in RAS1, thereby deactivating the projection technique. This allows to compute transition dipole moments (TDM) between valence and core-excited states via the RASSI module in OpenMolcas.³⁴

All quantum chemical calculations were performed with OpenMolcas³⁹ using the COBRAMM.⁴⁰ The core-excited calculations were performed on around 100 geometries constituting the two-dimensional grid used to perform the quantum dynamics simulations (see section "Wavepacket Simulations").

Due to the random nature of the definition of the wavefunction phase in quantum chemistry software, properties such as the TDM acquire discontinuities in their profiles when represented on a grid. This can affect the sign of contributions to the overall signal due to the Loop diagrams (Scheme 1b) where state indices e and e' differ. A wavefunction phase tracking protocol was therefore implemented in order to obtain continuous TDM profiles.

In the following, we outline the procedure on the example of a state i from the manifold of valence states e (i.e. e_i) and state a from the manifold of core-excited states f (i.e. f_a). At a reference geometry k (chosen at one of the grid's edges) the sign of the TDM $\langle e_i^k | r^k | f_a^k \rangle$ is established. Subsequently:

- a) the overlap matrix between valence states ($\langle e^k | e^{k'} \rangle$, dimensions 3×3) and between core-excited states ($\langle f^k | f^{k'} \rangle$, dimensions 30×30) at the reference geometry k and at an adjacent point k' is computed;
- b) state assignment at adjacent point k' is determined by means of maximum overlap;
- c) based on the signs of the maximum valence/valence $\langle e_i^k | e_j^{k'} \rangle$ and core-excited/core-excited $\langle f_a^k | f_b^{k'} \rangle$ overlaps at the two adjacent points, it is decided whether to retain or invert the sign of the TDM at geometry k' ; specifically, the sign is changed if only one of the overlaps is negative.

Next, geometry k' becomes the new reference geometry and steps a)-c) are repeated with the next point on the grid, while maintaining wavefunction sign bookkeeping.

Wavepacket Simulations

The geometries of the Franck-Condon (FC) point, of the S_2 minimum (S_2 min) and of the S_2/S_1 conical intersection (CoIn) were used to construct two nuclear degrees of freedom for our effective Hamiltonian.⁴¹ The first coordinate $\boldsymbol{\nu}_{\text{FC} \rightarrow \text{CoIn}}$ is the normalized displacement vector that points from the FC to the CoIn. $\boldsymbol{\nu}_{\text{FC} \rightarrow S_2 \text{min}}$ is the displacement vector from the FC to the local S_2 min which is then orthonormalized with respect to $\boldsymbol{\nu}_{\text{FC} \rightarrow \text{CoIn}}$.

All quantities, including the potential surfaces of the electronic states, non-adiabatic coupling between valence states, and transition dipole moments between valence and core-excited states were evaluated at around 100 nuclear grid points where the nuclear WP is energetically accessible. To accurately describe the nonadiabatic couplings near the CoIn area, we have used denser 26×20 grid points, spanning 0.5 to 1.0 \AA for $\boldsymbol{\nu}_{\text{FC} \rightarrow \text{CoIn}}$ and -0.15

to 0.15\AA for $\nu_{\text{FC} \rightarrow S_2\text{min}}$ reactive coordinates. The spiky nature of nonadiabatic coupling due to phase change across the CoIn is observed in Figure S1. Then all quantities are discretized on spatial 128×128 grid points in $\nu_{\text{FC} \rightarrow \text{CoIn}}$ and $\nu_{\text{FC} \rightarrow S_2\text{min}}$ by inter/extrapolation.

The nuclear dynamics are launched using a 20-fs full width at half-maximum (FWHM) Gaussian laser pump in resonance with the $S_0 \rightarrow S_2$ transition as was done experimentally,⁹

$$\epsilon(t) = A_2 e^{-\frac{(t-t_0)^2}{2\sigma^2}} \cos(\omega_{\text{pu}}(t - t_0)) \quad (15)$$

where $A_2 = 1.0 \times 10^{-2}$ a.u. is the electric field amplitude, giving the total intensity of 3.509×10^{12} W/cm², below the ionization limit. $\omega_{\text{pu}} = 3.89$ eV is the central frequency corresponding to the energy gap between the ground state and the S_2 state at the FC point, and $\sigma = 20$ fs is the temporal duration of the pump pulse. We used this intense pump field to obtain a considerable population in the S_2 . Qualitatively, we expect that the path of the nuclear wavepacket (WP) in the excited/ground state will not change substantially upon the decreasing pump intensity, even in the weak field limit. The nuclear WP is then propagated by numerically solving the time-dependent Schrodinger equation on the two-dimensional nuclear grid:⁴²

$$i\hbar \frac{\partial}{\partial t} \psi = \mathbf{H} \psi = \left[\mathbf{T}_\nu + \mathbf{V} - \boldsymbol{\mu} \epsilon(t) \right] \psi, \quad (16)$$

\mathbf{T}_ν is the kinetic energy operator of the nuclei in internal coordinates ν , \mathbf{V} is the potential energy operator, and $\boldsymbol{\mu} \epsilon(t)$ describes the light-matter interaction.

The Chebychev propagation⁴² with a 0.048 fs time step is employed to propagate this wavepacket until the final time of 242 fs. The G-matrix formalism⁴³ was employed to set up the kinetic energy operator,

$$\mathbf{T}_\nu \simeq -\frac{\hbar^2}{2m} \sum_{r=1}^M \sum_{s=1}^M \frac{\partial}{\partial \nu_r} \left[\mathbf{G}_{rs} \frac{\partial}{\partial \nu_s} \right] \quad (17)$$

with the G-matrix computed via its inverse elements

$$(G^{-1})_{rs} = \sum_{i=1}^{3N} m_i \frac{\partial \mathbf{x}_i}{\partial \boldsymbol{\nu}_r} \frac{\partial \mathbf{x}_i}{\partial \boldsymbol{\nu}_s} \quad (18)$$

For the 4TU coordinates, the G-matrix elements are $G_{\nu_r \nu_r} = 0.00007234 a.u.$, $G_{\nu_s \nu_s} = 0.00009237 a.u.$, and the kinetic coupling $G_{\nu_r \nu_s} = -0.00002765 a.u.$.

Our effective Hamiltonian was designed for describing the transition from the S_2 to the S_1 state and it may not accurately describe the WP propagation in S_1 since other nuclear degrees of freedom not included in our Hamiltonian become relevant. For example, in the vicinity of the S_1 minimum (S_1 min), the $T_{1/2}$ states are nearly isoenergetic. The wavepacket undergoes ISC, facilitated by a spin-orbit coupling. However, population of the triplet manifold from the S_2 or S_1 state cannot be described by our two-dimensional Hamiltonian since spin-orbit crossings are not readily accessible by the numerical protocol and the ISC may be facilitated along other modes. Hence, the ISC dynamics is described phenomenologically by absorbing the nuclear wavepacket at the S_1 min with a Butterworth filter operation⁴⁴ to prevent major artificial back-evolution to S_2 . The filter was of right-pass type and placed at $\boldsymbol{\nu}_{\text{FC} \rightarrow \text{CoIn}} = -0.15 a.u.$ with an order of 100.

We note that the same valence PES and non-adiabatic couplings were used in our previous study which focused on off-resonant spectroscopy simulations.²⁶ In an effort to render the simulations more realistic, here we use a realistic optical pump to initiate the dynamics. In the previous work the excited state wave packet was assumed to be created impulsively.

Results and discussion

First, we briefly describe the photoinduced $S_2 \rightarrow S_1$ IC dynamics. We simulate with reduced-dimensional nuclear quantum dynamics on a numerical grid spanned by the two reactive coordinates $\boldsymbol{\nu}_{\text{FC} \rightarrow \text{CoIn}}$ and $\boldsymbol{\nu}_{\text{FC} \rightarrow S_2 \text{ min}}$ describing the motion from the FC to the CoIn and to the S_2 min, respectively. The PESs of the relevant electronic states are displayed in Figure

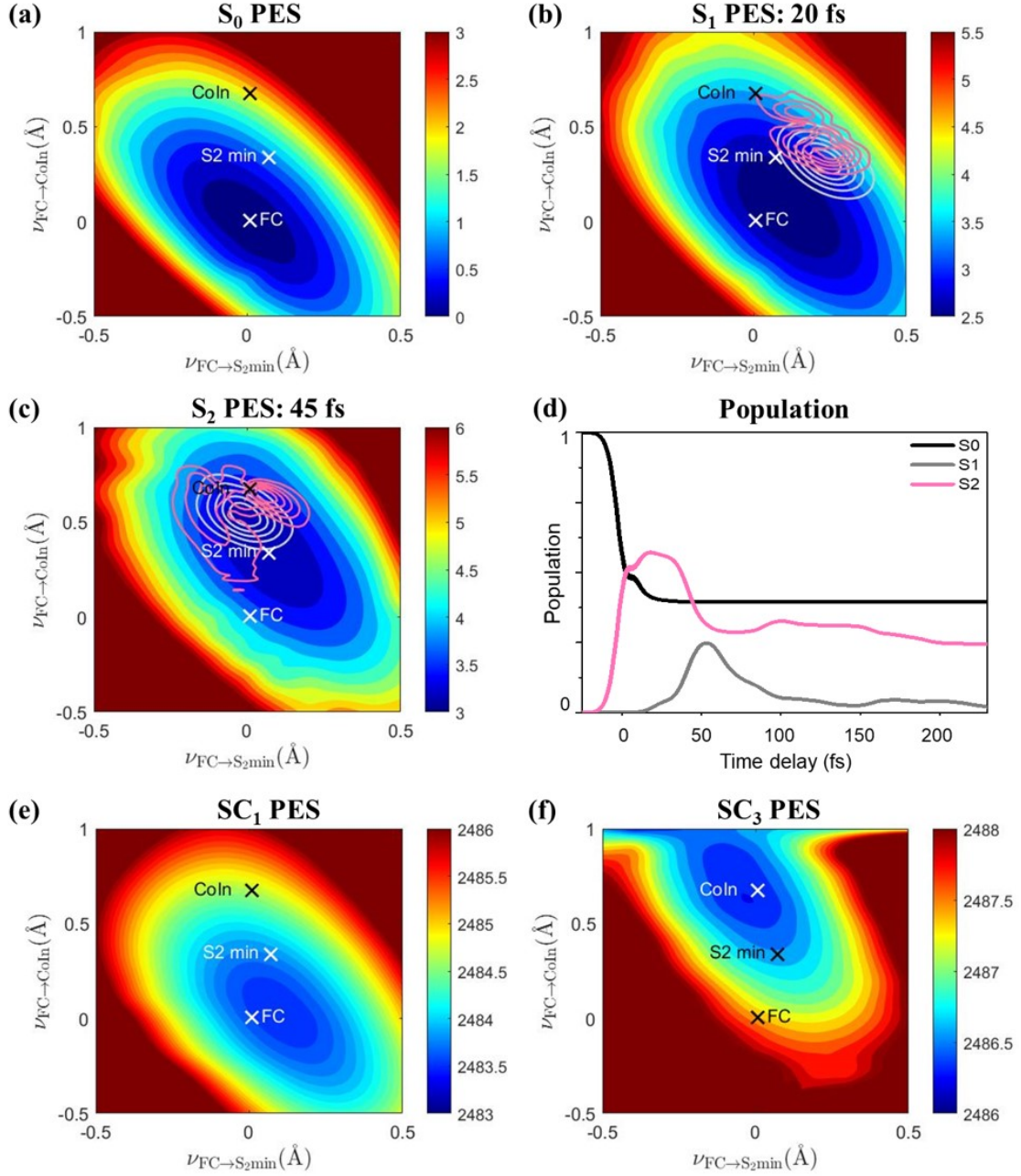


Figure 1: Potential energy surfaces and nuclear wavepacket dynamics: (a) S_0 PES, (b) S_1 PES with nuclear wavepacket at 20 fs, S_2 PES with the nuclear wavepacket at 45 fs, (d) state populations, (e) SC_1 PES, and (f) SC_3 PES. $T = 0$ is set to the maximum intensity of the 20-fs FWHM Gaussian pump. S_2 wavepacket (gray contours), S_1 wavepacket (pink contour). The SC_1 and SC_3 PES refer to the S K-edge core excited states which will be discussed in the main text. A movie including S_0 , S_1 , and S_2 PESs can be found in Figure S3.

1a-c. The S_2 PES exhibits a single well with a barrierless pathway from the FC to the S_2 min which is characterized by pronounced C₂–C₃ and C₄–S elongation. Toward the CoIn which lies 0.3 eV above the S_2 min and is nearly isoenergetic with the FC point, the C₂–C₃ is further elongated, in addition to planarity-conserving in-plane bending deformations of oxygen and vicinal hydrogens.

First, an optical UV pump pulse creates a population in the S_2 state. The WP starts from the FC region, then reaches the S_2 min in 20 fs (Figure 1b) and the CoIn in 45 fs (Figure 1c), resulting in relaxation to the S_1 and therefore simultaneous population of both electronic state, termed vibronic coherence. The S_2 WP evolves back to the FC region and oscillates between the FC and the CoIn with a 70 fs period. Both coordinates cooperatively deform the geometry of the molecule leading the nuclear WP from the FC region to the CoIn. The second coordinate, $\nu_{\text{FC} \rightarrow S_2 \text{min}}$ mainly facilitates decoherence between the excited state nuclear WPs due to the different energy gradient in both states. The S_1 and S_2 WP evolve differently after they arrive at the FC region and their overlap decreases over time.(Figure S3). Surface hopping simulations⁹ had reported characteristic C–S stretching (457 cm⁻¹) and ring breathing (697 and 783 cm⁻¹) modes associated with the dynamics on S_2 . The 70 fs (~ 476 cm⁻¹) WP oscillation period in the QD simulations matches nicely the C–S stretching mode period thereby demonstrating that the reduced vectors encompass projections on the modes relevant to the dynamics in S_2 . The S_1 WP moves away from the CoIn to the S_1 min, where the ISC mostly takes place. In order to mimic the ISC process, we absorb the parts of the nuclear WP which reach the S_1 min.

The S_2 population decay (Figure 1d) was fitted with $P(t) = Ae^{-t/k} + P_0$, where $P_0 + A$ is the initial population, yielding a time constant k of 52.4 fs, in agreement with our previous work (56 fs),²⁶ experiment (76 fs) and surface hopping simulations (67.5 fs).⁹

Before presenting the TRXAS signal, we discuss the core-excited electronic structure of 4TU for the various core atoms. Figure 2 shows the K-edges of sulfur, oxygen and nitrogen that can be obtained experimentally by near-edge X-ray absorption fine structure (NEXAFS)

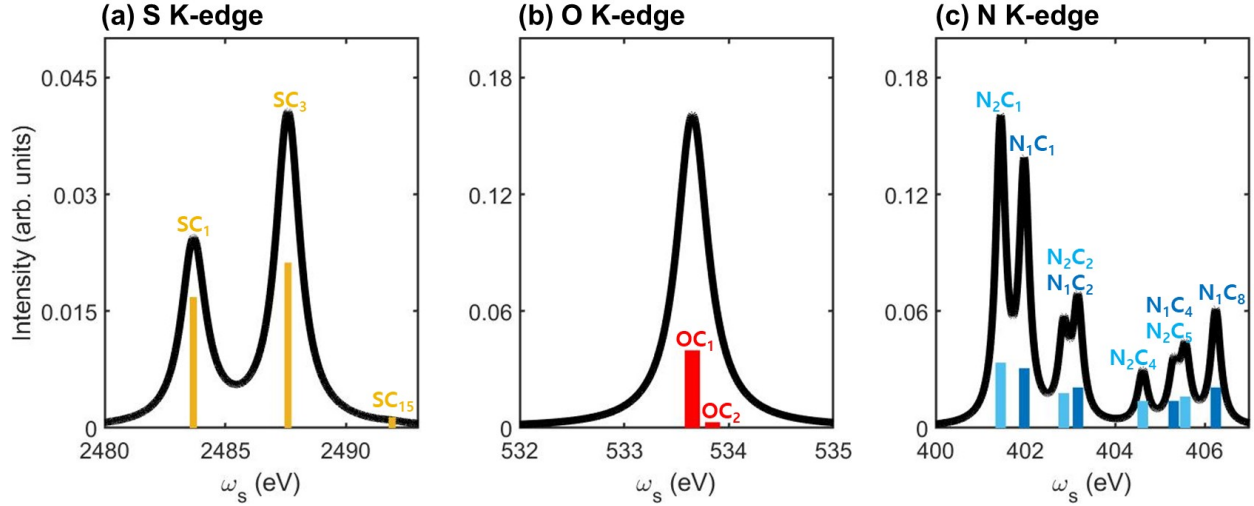


Figure 2: Near-edge X-ray absorption fine structure (Linear ground state X-ray absorption spectra) at (a) sulfur, (b) oxygen, and (c) nitrogen K-edges.

spectroscopy, a form of linear absorption spectroscopy. We recognize a fine pre-edge structure due to bright core-electron transitions to valence orbitals. Table 1 lists the energies, TDMs and orbitals involved in the said transitions. These are labeled SC_n , OC_n , N_1C_n , and N_2C_n , where n is ordered by increasing core state energies at the FC geometry. i.e., SC_1 indicates the lowest sulfur $1s$ core excited state.

The sulfur K-edge exhibits two peaks, at 2483.5 (SC_1) and 2487.5 eV (SC_3) (Figure 2a), associated with transitions from the $1s$ core orbital of sulfur into the vacant lowest unoccupied molecular orbital (LUMO) π_1^* and into a σ_2^* orbital, respectively (depicted in Figure 3a). These two orbitals have pronounced MO coefficients on the sulfur, in particular σ_2^* is the anti-bonding C-S orbital. This highlights an important requirement for core-transitions to be optically bright, namely that the arrival valence orbital must have a non-negligible contribution from basis functions on the atom hosting the $1s$ core-orbital (highlighted by a dashed cyan circles in Figure 3). In agreement with this requirement, the only bright transition in the K-edge of oxygen at 533.5 eV (OC_1) is associated with orbital π_2^* (depicted in Figure 3b), while the transition to the LUMO, having no MO coefficient on the oxygen, is dark. We note that also orbital π_3^* (see Figure S2 in the SI) shows a contribution on the oxygen giving rise to a weak band at 533.8 eV (OC_2 , Figure 2b). The nitrogen K-edge is

very rich with multiple peaks in the window 401.5-406.5 eV (Figure 2c) which is rationalized not only by the presence of two nitrogen atoms in 4TU but also by their contribution to orbitals $\pi\pi^*_{1-3}$ (depicted in Figure 3c).

The valence $\pi\pi^*$ and $n\pi^*$ states exhibit semi-vacant occupied orbitals labeled π_5 MO and n (Figure 3), that can act as arrival orbitals for the core-excited electrons, giving rise to additional signals in the transient X-ray spectra. Moreover, as occupied valence orbitals are energetically more stable than virtual ones, the transient signals are expected to be red-shifted by several eV in a background free pre-edge region making them particularly appealing for studying electronic states (ES) dynamics. As an example, the sulfur $1s \rightarrow n$ transition from the $n\pi^*$ state and the $1s \rightarrow \pi_5$ transition from the $\pi\pi^*$ state appear at 2480.5 ($n\pi^* \rightarrow \text{SC}_1$) and 2479.5 eV ($\pi\pi^* \rightarrow \text{SC}_1$), respectively, i.e. 3-4 eV below the lowest ground state absorption feature. In the nitrogen K-edge the $1s \rightarrow n$ transition from N₂ (i.e., the nitrogen next to the thiocarbonyl group) is weakly dipole allowed since the lone pair is partially delocalized over the vicinal atoms. The corresponding transition from N₁ is completely dark.

Further transitions into virtual orbitals, such as the sulfur $1s \rightarrow \sigma_2^*$ or nitrogen $1s \rightarrow \pi_1^*$ which could be also probed from the valence excited states, are expected to overlap with the corresponding absorption features from the ground state, giving rise to a complex pattern. For example, we had already established the $1s \rightarrow \pi_2^*$ transition is the only bright transition in the K-edge of oxygen. This transition can also be excited from the $n\pi^*$ and $\pi\pi^*$ state, giving rise to doubly excited hybrid states OC₅ and OC₈ with configurations $1s^{[1]}n^{[1]}\pi_1^{*[1]}\pi_2^{*[2]}$ and $1s^{[1]}\pi_5^{[1]}\pi_1^{*[1]}\pi_2^{*[2]}$ absorbing around 533.5 eV, thereby matching the energy of the $1s \rightarrow \pi_2^*$ from the ground state. We thus expect that transient and ground state absorption contribution should largely cancel out for K-edges of atoms not involved in the IC. On a side note, the presence of intense contributions in the transient spectra from doubly excited electronic states highlights the necessity to use multiconfigurational methods, capable of treating single and double excitations at equal footing, for a complete description the K-edge

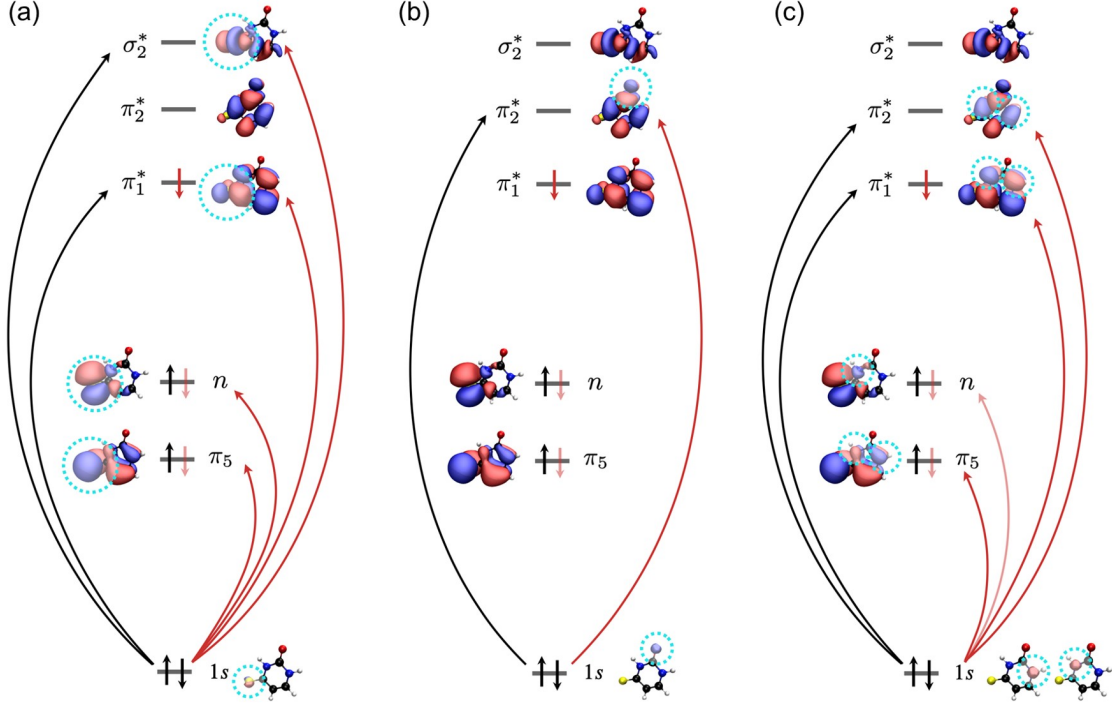


Figure 3: Core to valence transitions giving rise to features in the near-edge X-ray absorption fine structure (NEXAFS, Figure 2) and optical pump - resonant X-ray probe (TRXAS, Figure 4) spectra at (a) sulfur, (b) oxygen and (c) nitrogen K-edges. Core and valence orbitals are shown. Black and red lines denote transitions from the electronic ground (S_0) and valence excited (S_1 and S_2) states, respectively. Dashed cyan circles highlight valence orbitals of which contributions from the heteroatom involved in the core-excitation.

in the simulations. In density functional theory, these hybrid states are not straightforwardly accessible but can be described to some extent by coupling core-excited electronic structure calculations to the maximum overlap method which provides access to excited state self-consistent field solutions.^{25,45}

Valence State	K-edge	Root	ΔE (eV)	$ \mu $ (a.u.)	CSF (weight)
S_0	N1	N_1C_1	401.98	0.0307	$1s^{[1]}\pi_1^{*[1]}$ (75%)
S_0	N1	N_1C_2	403.17	0.0208	$1s^{[1]}\pi_2^{*[1]}$ (69%)
S_0	N1	N_1C_4	405.31	0.0139	$1s^{[1]}\pi_5^{[1]}\pi_1^{*[2]}$ (61%)
S_0	N1	N_1C_8	406.25	0.0208	$1s^{[1]}\pi_3^{*[1]}$ (41%)

S_0	N2	N_2C_1	401.45	0.0335	$1s^{[1]}\pi_1^{*[1]}$ (77%)
S_0	N2	N_2C_2	402.86	0.0179	$1s^{[1]}\pi_2^{*[1]}$ (69%)
S_0	N2	N_2C_4	404.62	0.0139	$1s^{[1]}\pi_5^{[1]}\pi_1^{*[2]}$ (56%)
S_0	N2	N_2C_5	405.57	0.0162	$1s^{[1]}\pi_5^{[1]}\pi_1^{*[1]}\pi_2^{*[1]}$ (38%) $1s^{[1]}\sigma_1^{*[1]}$ (23%)
S_0	O	OC_1	533.65	0.0399	$1s^{[1]}\pi_2^{*[1]}$ (68%)
S_0	S	SC_1	2483.68	0.0168	$1s^{[1]}\pi_1^{*[1]}$ (90 %)
S_0	S	SC_3	2487.60	0.0212	$1s^{[1]}\sigma_2^{*[1]}$ (81 %)
<hr/>					
$S_1(n\pi^*)$	N1	N_1C_3	401.67	0.0249	$1s^{[1]}n^{[1]}\pi_1^{*[2]}$ (85%)
$S_1(n\pi^*)$	N1	N_1C_5	402.74	0.0191	$1s^{[1]}n^{[1]}\pi_1^{*[1]}\pi_2^{*[1]}$ (91%)
$S_1(n\pi^*)$	N2	N_2C_1	398.50	0.0090	$1s^{[1]}\pi_1^{*[1]}$ (77%)
$S_1(n\pi^*)$	N2	N_2C_3	401.82	0.0242	$1s^{[1]}n^{[1]}\pi_1^{*[2]}$ (89%)
$S_1(n\pi^*)$	N2	N_2C_6	402.96	0.0208	$1s^{[1]}n^{[1]}\pi_1^{*[1]}\pi_2^{*[1]}$ (90%)
$S_1(n\pi^*)$	O	OC_5	533.70	0.0393	$1s^{[1]}n^{[1]}\pi_1^{*[1]}\pi_2^{*[1]}$ (55%)
$S_1(n\pi^*)$	S	SC_1	2480.73	0.0235	$1s^{[1]}\pi_1^{*[1]}$ (90 %)
$S_1(n\pi^*)$	S	SC_{13}	2489.14	0.0172	$1s^{[1]}n^{[1]}\sigma_2^{*[1]}\pi_1^{*[1]}$ (62 %)
<hr/>					
$S_2(\pi\pi^*)$	N1	N_1C_1	397.76	0.0191	$1s^{[1]}\pi_1^{*[1]}$ (75%)
$S_2(\pi\pi^*)$	N1	N_1C_4	401.09	0.0279	$1s^{[1]}\pi_5^{[1]}\pi_1^{*[2]}$ (61%)
$S_2(\pi\pi^*)$	N1	N_1C_8	402.03	0.0110	$1s^{[1]}\pi_3^{*[1]}$ (41%)
$S_2(\pi\pi^*)$	N1	N_1C_9	402.59	0.0069	$1s^{[1]}\pi_5^{[1]}\pi_1^{*[1]}\pi_2^{*[1]}$ (30%)
$S_2(\pi\pi^*)$	N2	N_2C_1	397.23	0.0226	$1s^{[1]}\pi_1^{*[1]}$ (77%)
$S_2(\pi\pi^*)$	N2	N_2C_4	400.40	0.0249	$1s^{[1]}\pi_5^{[1]}\pi_1^{*[2]}$ (56%)
$S_2(\pi\pi^*)$	O	OC_8	533.62	0.0376	$1s^{[1]}\pi_5^{[1]}\pi_1^{*[1]}\pi_2^{*[1]}$ (45%)

$S_2(\pi\pi^*)$	S	SC ₁	2479.46	0.0157	$1s^{[1]}\pi_1^{*[1]}$ (90%)
$S_2(\pi\pi^*)$	S	SC ₃	2483.38	0.0099	$1s^{[1]}\sigma_2^{*[1]}$ (81%)
$S_2(\pi\pi^*)$	S	SC ₁₅	2487.70	0.0155	$1s^{[1]}\pi_3^{[1]}\sigma_2^{*[1]}\pi_1^{*[1]}$ (37%)

Table 1: Transition energies (eV) and dipole moments (a.u.) between valance (labelled S_0 , S_1 , and S_2) and core-excited states (labelled $X_{(n)}C_n$ for sulfur, oxygen and both nitrogen atoms of 4TU at the FC point geometry. Leading configuration state functions (CFS) and corresponding weights are also shown.

Next, we present the optical pump - resonant X-ray probe TRXAS signals represented by the Loop diagram given in Scheme 1b from an ensemble of randomly oriented molecules. We use a single broadband probe pulse (Scheme 1, 15 eV bandwidth) and tune its central frequency to the sulfur (2483.5 eV), oxygen (533.5 eV), and nitrogen (402 eV) K-edges. The signals were computed using eqn. 13 in the x, y and z polarization direction in the molecular frame and then rotationally averaged with a second rank tensor, leading to

$$\langle S(\omega_s, T) \rangle_\Omega = \frac{1}{3} [S_{xx}(\omega_s, T) + S_{yy}(\omega_s, T) + S_{zz}(\omega_s, T)] \quad (19)$$

where $S_{xx/yy/zz}$ represents the optical pump - resonant X-ray probe signal calculated with x/y/z components of transition dipoles (i.e., $\mu_{e'f,x}$ and $\mu_{fe,x}^\dagger$), respectively.

The signals calculated at the three K-edges are displayed in Figure 4a-c upper left panel, respectively, showing positive (red) and negative (blue) contributions. In agreement with the preceding discussion, the negative peaks arise from the ground state absorption to SC₁ (2483.7 eV), SC₃ (2487.5 eV) for sulfur K-edge, OC₁ (at 533.5 eV) for oxygen K-edge, etc. (also know as ground state bleach, GSB) and constitute a steady background. Positive contributions arise due to photoinduced absorption (PA) from transiently populated valence excited states which exhibit rise and decay in response to the electronic dynamics while simultaneously modulated by oscillatory features due to vibrational dynamics.

Herein, we emphasize that the S_2/S_1 PESs have mainly $\pi\pi^*/n\pi^*$ electronic character,

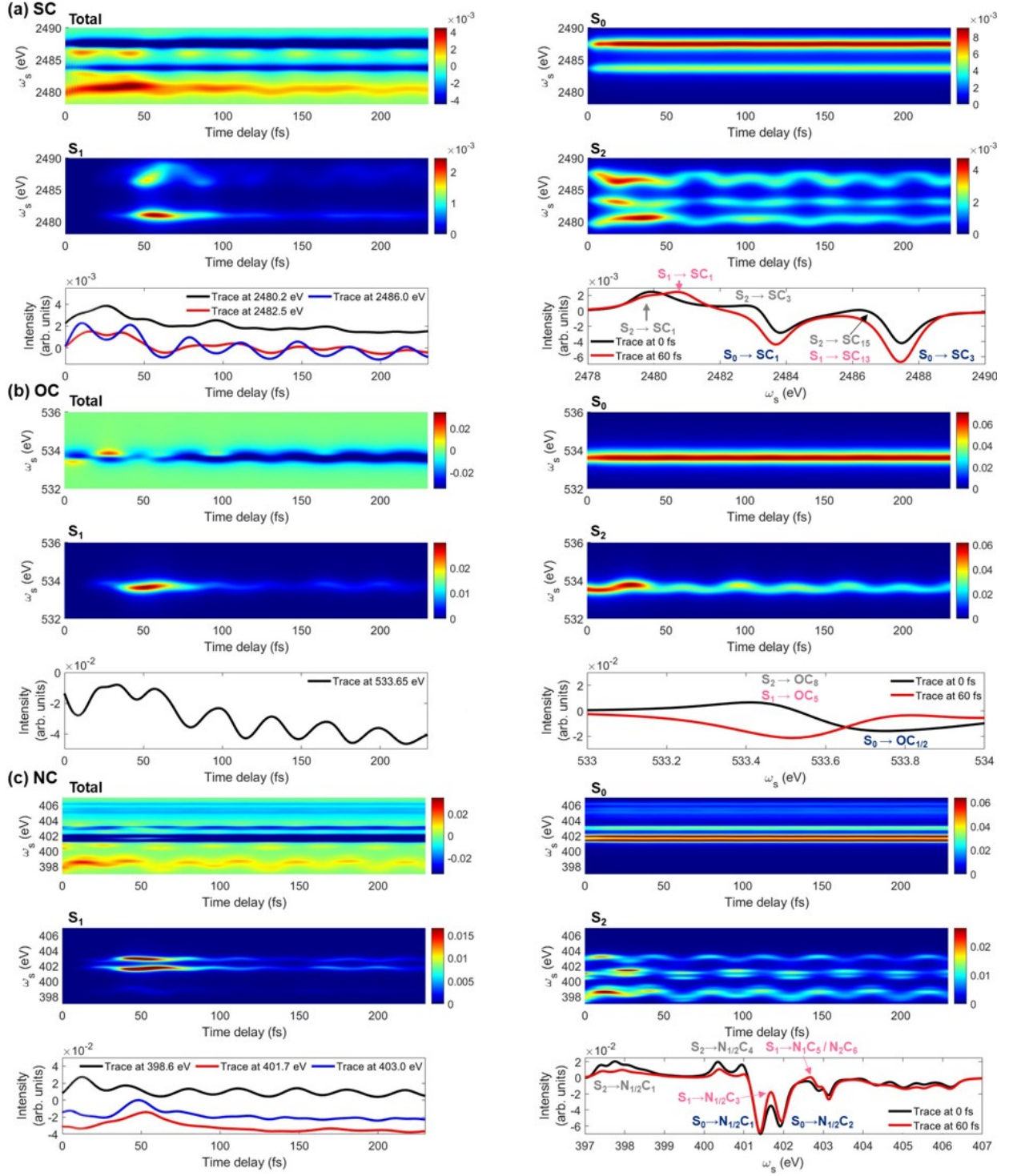


Figure 4: Simulated optical pump - X-ray probe signals of 4TU calculated with single broad-band probe field at (a) sulfur, (b) oxygen, and (c) nitrogen K-edges. The top and middle panels show the total signal (top left) and the contribution to the total signal from each valence state. The negative contribution in the total signal comes from the ground state bleach background. The bottom panels show the temporal (left) and spectral (right) trace of the total signal (Black, red, and blue) at certain detection frequency and time delay, respectively. The navy, pink, and gray arrows and texts indicate the involved electronic transition from the S_0 , S_1 , and S_2 valence state to the core manifold, respectively

respectively. Genereally, the electronic character switches across the CoIn, e.g., S_2 PES exhibits the $\pi\pi^*$ character before crossing the CoIn, but $n\pi^*$ character thereafter. However, in 4TU, where the electronic energies at the FC and the CoIn are similar, the WP can not cross over the CoIn area but bounces back to the FC point. The nuclear WP is predominantly propagated before the CoIn at all times, with only very minor parts actually crossing the CoIn. We thus cautiously discuss the photoinduced absorption from the S_2 and the S_1 using $\pi\pi^*/n\pi^*$ nomenclature, even though we did not perform an explicit diabaticization.

The SC_1 signal at 2480 eV is the only core-excited state which is simultaneously bright from both $\pi\pi^*$ and $n\pi^*$ excited states since the relevant transition densities are localized on the sulfur. The signal rises immediately after the S_2 is populated and remains strong even upon CoIn passage as the decrease of S_2 population is compensated by the increase of S_1 population, i.e. the decay of the $\pi\pi^*$ contribution coincides with the rise of the $n\pi^*$ absorption (Figure 4a, middle panels). After the CoIn passage, the S_2 and S_1 nuclear WPs propagate in their respective PESs with finite splitting. The spectral trace at 60 fs at the bottom right panel (red lines) exhibits the double peak structure due to the PA coming from the $\pi\pi^*$ (gray) and the $n\pi^*$ (pink). The PA signal splitting clearly shows signatures of the bifurcation of the coherent nuclear WP. The SC_3 and SC_{15} states are fingerprint PA features of $\pi\pi^*$. The SC_{13} state, in contrast, is dipole allowed only from $n\pi^*$, thus is observable only when the nuclear WP reaches CoIn area (after 45 fs) and the S_1 state, exhibiting $n\pi^*$ character have significant populations. Note, however, that the spectral overlap of SC_{13} and SC_{15} makes it hard to resolve the $n\pi^*$ contributions from the $\pi\pi^*$ ones in the sulfur K-edge.

All PA signals in the sulfur K-edge exhibit quantum beating (i.e. coherent intensity oscillations) of which intensity oscillation depends on the vibrational coordinate, the transfer of population to other states with varying transition dipole moments along the grid, and the different electronic character of the core states. First, the quantum beat originating from the vibration coordinate can be observed from the fact that the intensity oscillation is repeated with the period of 70 fs, corresponding to the C–S stretching mode of our reactive

coordinates. The population transfer to the S_1 state, which has mainly $n\pi^*$ character, and thus its dark TDM against SC_3 state, make the quantum beat at 2482.5 eV strong in the beginning (bottom left panel in Figure 4a) when the nuclear WP is localized at the FC point, but weaker after the nuclear WP reaches the CoIn area. In contrast, the quantum beat at 2480.2 eV (transition to SC_1) is strongest between 20 to 40 fs, when the nuclear WP passes by the S_2 min and the CoIn area, where the large transition dipole moment between the S_1 and SC_1 state can contribute to the PA. Finally, the SC_1 band differs from the patterns of the $SC_{3/13/15}$ bands. In particular, we see a red-shift of the $SC_{3/13/15}$ signals during the motion toward the CoIn and a blue-shift during the motion away from it. The opposite trend is observed for the SC_1 signal. States $SC_{3/13/15}$ have in common a transition into the σ_2^* localized on the C–S bond. Due to the anti-bonding nature of the orbital, the core-excited PES exhibits its minimum at elongated C–S, i.e. in the direction of the CoIn (Figure 1f). Thus, during the motion of the WP toward the CoIn, the valence-to-core-excited energy gap decreases leading to the observed red-shift of the PA. In SC_1 the core-electron is brought away from the sulfur into a π^* orbital delocalized over the entire ring which leads to a decrease of the nuclear charge shielding around the sulfur. This causes the heteroatom to withdraw electron density from the nearby carbon strengthening the bond. As a consequence the C–S bond shortens at the SC_1 PES minimum (Figure 1e). Thus, during the WP motion toward the CoIn, the valence-to-core-excited energy gap increases, which translates into a blue-shift of the PA. Thus, the pump-probe signal provides spectroscopic signatures of the relevant nuclear motion on the PES which can be extracted by first subtracting the electronic dynamics, itself accessible through global fitting, and subsequently Fourier transforming the residuals.^{6,9}

As discussed above, for the oxygen K-edge (Figure 4b), the lowest core excited state is not dipole allowed from the valence excited states but accessible from the ground state. Its oscillator strength is too weak to be visible in the spectra since the oxygen atom only makes a minor contribution to π_5 and to the sulfur lone pair. $n\pi^*$ and $\pi\pi^*$ have one particu-

larly bright core-excited state each, labeled OC_5 and OC_8 , respectively, associated with the $1s \rightarrow \pi_2^*$ transition, that has a non-vanishing molecular orbital component on the oxygen atom. We note that the GSB and PA largely cancel out as the oxygen is insensitive to the molecular deformation along the 2D grid, confirming our expectation based on the analysis of the FC electronic structure. The valence to core-excited gap remains relatively constant throughout the grid, with a value of ca. 533.5 eV. While not being informative about the IC, it demonstrates how non-reactive groups generate a steady transient PA that shows no spectral dynamics.

For the nitrogen K-edge (Figure 4c), while we are in the position to computationally distinguish core-transitions from either N_1 or N_2 , we note that for broadband-probe TRXAS, signals from both atoms will be observed simultaneously. The lowest core states, N_1C_1 and N_2C_1 , are well separated from higher ones and GSB, yielding the positive PA signatures. They exhibit strong resonances at 398 to 399 eV due to their large transition dipole moments from the $\pi\pi^*$ state, while the $n\pi^*$ contribution is weak and negligible. Accordingly, the signals intensities decrease when the nuclear WP passes through the CoIn at 45 fs (Bottom left panel in Figure 4c, black line). Hence, the lowest nitrogen core states provide spectral fingerprints for extracting the $\pi\pi^*$ lifetime. On a side note, we bring to the reader’s attention that the intensity decrease of a PA signal is not necessarily the consequence of population transfer to another state as it could be the result of decrease of the TDM along the grid for a given electronic state. To demonstrate this, Figure S5 shows plots of the TDM magnitude along the grid, evidencing that some transitions exhibit multifold variations of the TDM strength (e.g. $S_2 \rightarrow \text{N}_1\text{C}_4$) that would translate in fluctuations of the peak intensity even in adiabatic dynamics.

PA features from the $n\pi^*$, arises at around 401.7 eV (N_1C_3 and N_2C_3) and 403.0 eV (N_1C_5 and N_2C_6). The N_1 and N_2 absorption lines overlap giving a distinctive strong absorption line with a delayed rise. By taking the temporal trace at 401.7 and 403.0 eV, marked by the red and the blue line at the bottom left panel, one could retrieve the PA signature from

the $n\pi^*$ through the depletion of the GSB. Note that the GSB marks the steady background due to the localized nuclear WP at the S_0 PES.

We would expect to observe PA signatures of the triplet state rising on a several hundred femtosecond timescale following the ISC.⁹ Note that, while the triplet state has a characteristic PA in the Vis, the $n\pi^*$ state is dark and its involvement in the photophysics of 4TU has been inferred only indirectly, based on the mismatch between the decay of the SE from the $\pi\pi^*$ and the rise of the triplet PA.⁹ The TRXAS simulations show that the nitrogen K-edge is well suited to track the population dynamics in both the $\pi\pi^*$ and the $n\pi^*$ states.

The TRXAS signal involves both excited/ground state absorption ($e = e'$) and Raman transition components ($e \neq e'$) which are relevant to the electronic coherence. The requirements for strong coherence contributions can be inferred from eqs. 13: a) comparable populations in both valence states e and e' with overlapping WP; b) core-excited states that are dipole allowed simultaneously from both valence states; c) parallel or anti-parallel orientation of the corresponding TDMs. We found that for the oxygen K-edge (Figure 5b) the S_2/S_1 coherence is extremely weak (three orders smaller than populations) since each valence state is coupled to a different core-excited state. The sulfur (Figure 5a) and nitrogen K-edge (Figure 5c), in contrast, exhibit contributions from electronic coherences in the spectra which are only an order of magnitude less intense than contributions from populations as there are core-excited transitions which are dipole allowed from more than one state. The S_2/S_0 coherence in sulfur K-edge is observed at 2480, 2483.7, and 2487 eV through the SC_1 , SC_3 , and SC_{15} core states, respectively. They are strong in the beginning of the simulation when the S_2 WP is localized at the FC region since the S_2/S_0 overlap is maximal. With the evolution of the WP away from the FC the overlap decreases and eventually vanishes completely. To visualize the dynamical evolution of this frequency, we display an integrated Wigner spectrogram of temporal traces $S(T)$ of the coherence contribution over $\omega_s = 2477.2$ eV to 2492.4 eV in Figure 5g.

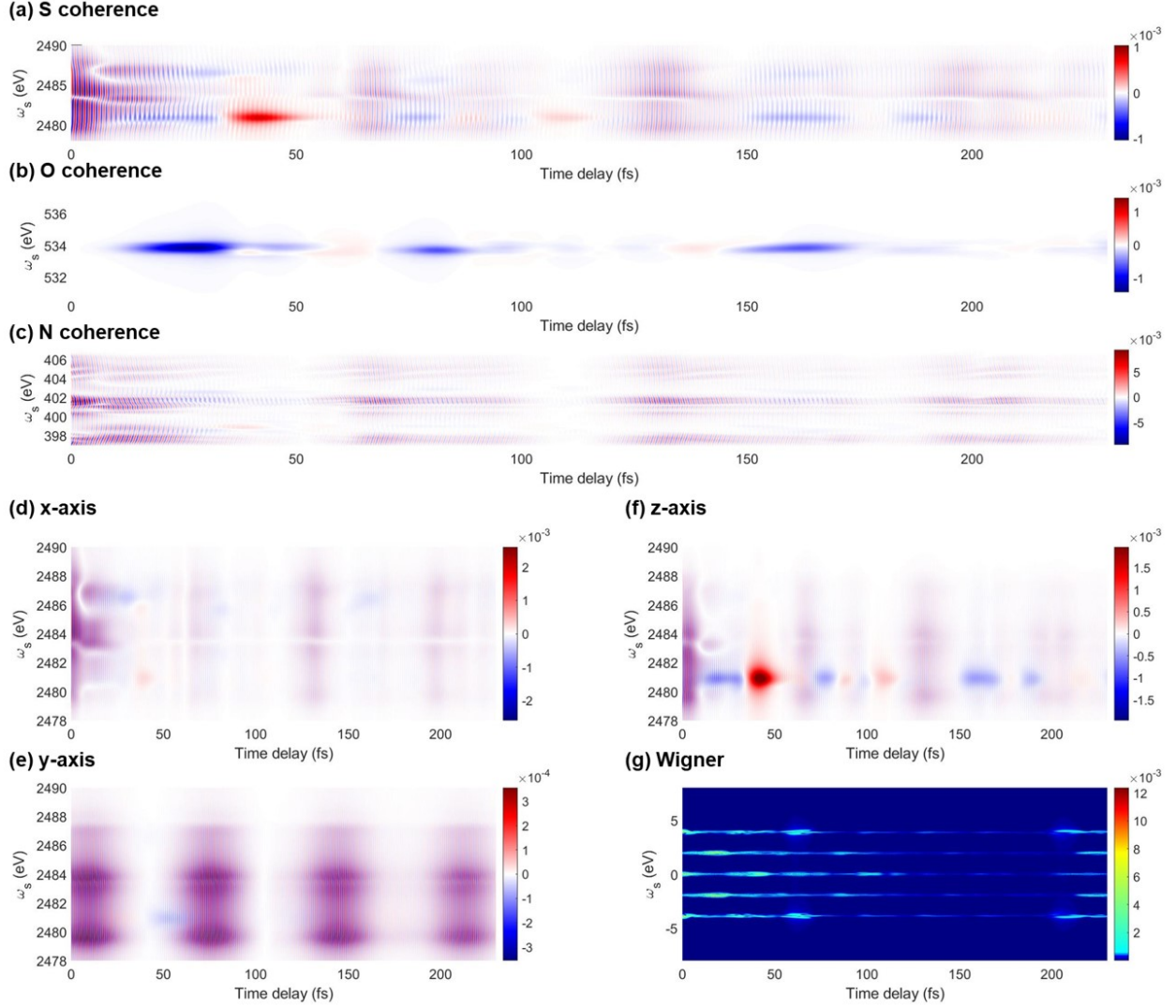


Figure 5: The coherence contribution to the total signal at (a) sulfur, (b) oxygen, and (c) nitrogen K-edges. The bottom panels d-f represents the coherence contribution to the sulfur K-edge signal along (d) x-axis (e) y-axis, and (f) z-axis. (g) The Wigner spectrogram integrating the temporal trace $S(t)$ of the signal over $\omega_s = 2477.2$ to 2492.4 eV.

$$W(T, \omega_{\text{coh}}) = \int_{-\infty}^{\infty} d\tau S(T + \tau) S(T - \tau) e^{i\omega_{\text{coh}}\tau}. \quad (20)$$

The main feature appears around 4 eV which coincides with the energy gap between the ground state and the S_2 state. A weak S_2/S_1 coherence contribution is observed at 2481 eV due to the finite TDM between the valence excited states and SC_1 but is masked by the population background, making it hard to extract. The SC_1 state is dipole allowed from both

$\pi\pi^*$ and $n\pi^*$, but actually the corresponding TDMs along y and z axes are orthogonal to each other (see their opposite phase at 2481 eV in Figure 5e and f). Due to the weak excitation by the y -linearly-polarized pump, the S_2/S_1 coherence survives and can be observed. Otherwise, their orthogonality leads to a vanishing coherence intensity after rotational averaging. The S_2/S_1 coherence appears in the Wigner spectrogram at 45 fs at around 0 eV and gives the approximate timing of the S_2/S_1 CoIn passage. A similar argumentation can be applied to nitrogen K-edge.

In the following, we show that the use of a hybrid narrow/broadband field provides a similar information with a narrower detection window, providing a specific single core state information. A femtosecond narrowband pulse \mathcal{E}_N excites a system on a valence electronic state $|e\rangle$ into a core level $|f\rangle$. Then, the attosecond broadband \mathcal{E}_B stimulates the emission. The inverse setup in which a broadband pulse is used to excite the system into a core level $|f\rangle$ whereas stimulated emission is realized by a narrowband pulse gives identical information. In both setups the detection window is limited by the narrowband whereas the attosecond broadband pulse proves the temporal resolution. The relevant pulse configuration and loop diagram are shown in Figure S6.

The narrowband pulse ω_N with 0.6 eV bandwidth was scanned over the sulfur K-edge between 2475 to 2490 eV to find the resonances. This bandwidth corresponds to the narrowest spectral resolution of XFEL with central frequency of 2 keV that can be gained with the current free-electron laser technology to the best of our knowledge. Eqn 14 indicates that the detected signal is centered at the narrowband central frequency ω_N due to the resonance condition. Otherwise, the term $e^{i(\omega_N - \omega_f)t_1}$ rapidly oscillates along t_1 which makes the integration over t_1 vanish.

In Figure 6a-c we represent the signal at $\omega_N = 2480.2$, 2483.2, and 2485.8 eV associated with transitions to SC_1 , SC_3 , and $SC_{13/15}$. One can selectively probe the time-evolving spectral signature of a core-to-valence transition at a given detection frequency. Using a broader incoming X-ray pulse (e.g. 4 eV) would allow to monitor time-evolving absorption lines of

several core states (e.g. SC_1 and SC_3) at the same time. We note that simulating the hybrid pulse TRXAS is identical to taking the temporal trace of the of the TRXAS simulated with a single broadband pulse in a 0.6 eV wide frequency window (compare the left and the right panels in Figure 6). For example, the double peak nature observed for $SC_{13/15}$ at 2485.8 eV is well represented in Figure 6c.

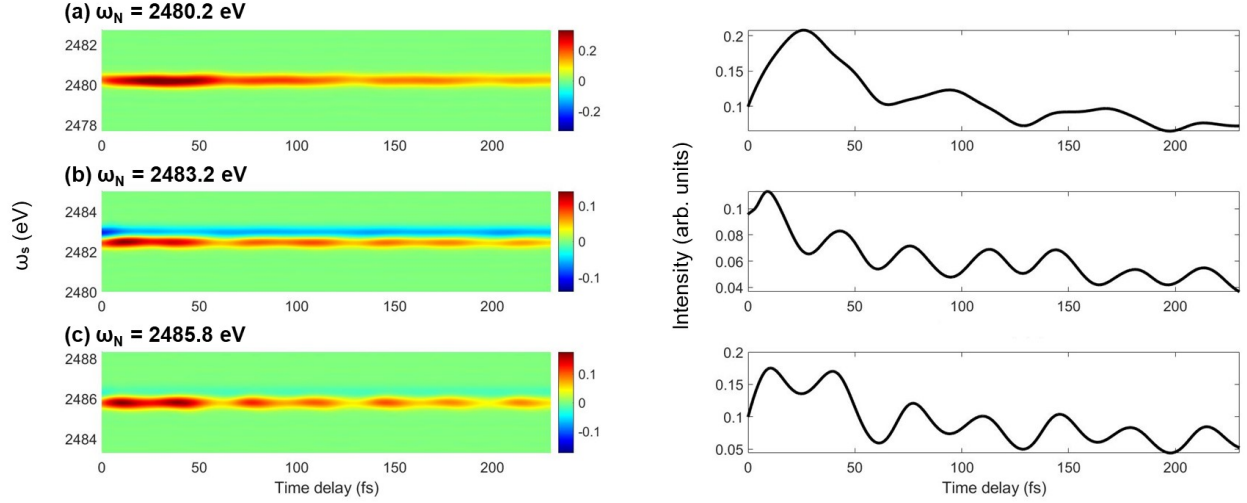


Figure 6: Optical pump - resonant X-ray probe signal calculated with hybrid field (left) for S K-edge at $\omega_N =$ (a) 2480.2 eV, (b) 2483.2 eV, and (c) 2485.8 eV. The temporal trace of the signal calculated with single broadband at the same central frequency is given at the right panels.

Conclusions

We have simulated the optical pump - resonant X-ray probe (TRXAS) signals which monitor the $\pi\pi^* \rightarrow n\pi^*$ internal conversion process in 4TU. Exact quantum nuclear wavepacket dynamics performed on a two-dimensional PES grid reproduces the relaxation dynamics in good agreement with experiment. A multiconfigurational wavefunction based protocol using restricted active space self-consistent field and multi-reference perturbation theory (RASSCF/RASPT2) allows access to electronic structure of the core-excited manifold with high accuracy. Treatment of single core-excited and double hybrid (core+valence)-excited

states on an equal footing assures the completeness of the transient spectra. The high-level electronic structure method reveals the characteristics of 4TU where the S_2/S_1 PES is dominated by the $\pi\pi^*/n\pi^*$ electronic character, due to the similar potential energy at the FC and the CoIn.

The simulated signals for various K-edges provide element-specific photoinduced absorption fingerprints of the $\pi\pi^*$ and $n\pi^*$ states. The lowest sulfur K-edge shows a strongly coherently oscillating resonance which is dipole allowed from both $\pi\pi^*$ and $n\pi^*$ states in a background-free pre-edge window. The oxygen K-edge is not sensitive to the molecular deformations and, as a consequence, exhibits a steady spectrum of strongly overlapping GSB and PA contributions. The lowest nitrogen PA marks the fingerprint of the $\pi\pi^*$ state and the decay of its intensity gives an approximate timing for the CoIn passage. Notably, an intense $n\pi^*$ spectral signature can be observed around 402 to 403 eV, facilitating the direct observation of its delayed population and the timing of the ISC. The $\pi\pi^*/n\pi^*$ electronic coherence is weak and covered by the much stronger population contributions.

In conclusion, TRXAS provides complementary information to off-resonant techniques such as TRUECARS by resolving the time scale of IC and ISC. The resonant technique is not suitable for resolving coherences built upon CoIn passage, thus emphasizing the need for off-resonantly tuned X-ray pulses to separate electronic coherences from population contributions. Substituting the single attosecond broadband probe pulse into a hybrid narrow/broadband field allows to probe individual core states separately but does not provide additional insights into the photophysics thus its implementation is discouraged.

Acknowledgement

This work was primarily supported by the U.S. Department of Energy, Office of Science, Office of Basic Energy Sciences under Award DE-SC0019484 (S. M. and M. G.). The support of the National Science Foundation through Grant No.CHE-1953045 is gratefully acknowl-

edged. Y. N. acknowledges support from the Korea Initiative for fostering University of Research and Innovation Program of the National Research Foundation (NRF) funded by the Korean government (MSIT) (No. 2020M3H1A1077095). D.K. gratefully acknowledges support from the Alexander von Humboldt foundation through the Feodor Lynen program.

Supporting Information Available

Electronic Supplementary Information (ESI) available: Loop diagram rule; Supplementary figures: The nonadiabatic coupling map, the active space, the nuclear wavepacket molecular dynamics movie, time-evolving electronic states levels, transition dipole moment maps, pulse configuration and loop diagram for hybrid X-ray probe pulse.

References

- (1) Maiuri, M.; Garavelli, M.; Cerullo, G. Ultrafast Spectroscopy: State of the Art and Open Challenges. *J. Am. Chem. Soc.* **2020**, *142*, 3–15, PMID: 31800225.
- (2) Conti, I.; Cerullo, G.; Nenov, A.; Garavelli, M. Ultrafast Spectroscopy of Photoactive Molecular Systems from First Principles: Where We Stand Today and Where We Are Going. *J. Am. Chem. Soc.* **2020**, *142*, 16117–16139, PMID: 32841559.
- (3) Buchner, F.; Nakayama, A.; Yamazaki, S.; Ritze, H.-H.; Lübcke, A. Excited-State Relaxation of Hydrated Thymine and Thymidine Measured by Liquid-Jet Photoelectron Spectroscopy: Experiment and Simulation. *J. Am. Chem. Soc.* **2015**, *137*, 2931–2938, PMID: 25671554.
- (4) Brister, M. M.; Crespo-Hernández, C. E. Excited-State Dynamics in the RNA Nucleotide Uridine 5-Monophosphate Investigated Using Femtosecond Broadband Transient Absorption Spectroscopy. *J. Phys. Chem. Lett.* **2019**, *10*, 2156–2161.

- (5) Erickson, B. A.; Heim, Z. N.; Pieri, E.; Liu, E.; Martinez, T. J.; Neumark, D. M. Relaxation Dynamics of Hydrated Thymine, Thymidine, and Thymidine Monophosphate Probed by Liquid Jet Time-Resolved Photoelectron Spectroscopy. *J. Phys. Chem. A* **2019**, *123*, 10676–10684, PMID: 31756106.
- (6) Borrego-Varillas, R.; Nenov, A.; Kabaciński, P.; Conti, I.; Ganzer, L.; Oriana, A.; Jaiswal, V.; Delfino, I.; Weingart, O.; Manzoni, C.; Rivalta, I.; Garavelli, M.; Cerullo, G. Tracking excited state decay mechanisms of pyrimidine nucleosides in real time. *Nat. Commun.* **2021**, *12*, cited By 0.
- (7) Sánchez-Rodríguez, J. A.; Mohamadzade, A.; Mai, S.; Ashwood, B.; Pollum, M.; Marquetand, P.; González, L.; Crespo-Hernández, C. E.; Ullrich, S. 2-Thiouracil intersystem crossing photodynamics studied by wavelength-dependent photoelectron and transient absorption spectroscopies. *Phys. Chem. Chem. Phys.* **2017**, *19*, 19756–19766.
- (8) Mai, S.; Mohamadzade, A.; Marquetand, P.; González, L.; Ullrich, S. Simulated and Experimental Time-Resolved Photoelectron Spectra of the Intersystem Crossing Dynamics in 2-Thiouracil. *Molecules* **2018**, *23*.
- (9) Borrego-Varillas, R.; Teles-Ferreira, D. C.; Nenov, A.; Conti, I.; Ganzer, L.; Manzoni, C.; Garavelli, M.; Maria de Paula, A.; Cerullo, G. Observation of the Sub-100 Femtosecond Population of a Dark State in a Thiobase Mediating Intersystem Crossing. *J. Am. Chem. Soc.* **2018**, *140*, 16087–16093.
- (10) Teles-Ferreira, D. C.; Conti, I.; Borrego-Varillas, R.; Nenov, A.; Van Stokkum, I. H. M.; Ganzer, L.; Manzoni, C.; de Paula, A. M.; Cerullo, G.; Garavelli, M. A Unified Experimental/Theoretical Description of the Ultrafast Photophysics of Single and Double Thionated Uracils. *Chem. Eur. J.* **2020**, *26*, 336–343.
- (11) Pollum, M.; Lam, M.; Jockusch, S.; Crespo-Hernández, C. E. Dithionated Nucle-

- obases as Effective Photodynamic Agents against Human Epidermoid Carcinoma Cells. *ChemMedChem* **2018**, *13*, 1044–1050.
- (12) Meisenheimer, K. M.; Koch, T. H. Photocross-Linking of Nucleic Acids to Associated Proteins. *Crit. Rev. Biochem. Mol. Biol.* **1997**, *32*, 101–140.
- (13) Favre, A.; Moreno, G.; Blondel, M.; Kliber, J.; Vinzens, F.; Salet, C. 4-thiouridine photosensitized RNA-protein crosslinking in mammalian cells. *Biochem. Biophys. Res. Commun.* **1986**, *141*, 847–854.
- (14) Reichardt, C.; Guo, C.; Crespo-Hernández, C. E. Excited-State Dynamics in 6-Thioguanosine from the Femtosecond to Microsecond Time Scale. *J. Phys. Chem. B* **2011**, *115*, 3263–3270, PMID: 21384813.
- (15) Pellegrini, C.; Marinelli, A.; Reiche, S. The physics of x-ray free-electron lasers. *Rev. Mod. Phys.* **2016**, *88*, 015006.
- (16) Chergui, M.; Collet, E. Photoinduced Structural Dynamics of Molecular Systems Mapped by Time-Resolved X-ray Methods. *Chem. Rev.* **2017**, *117*, 11025–11065.
- (17) Chen, L. X.; Zhang, X. Photochemical Processes Revealed by X-ray Transient Absorption Spectroscopy. *J. Phys. Chem. Lett.* **2013**, *4*, 4000–4013.
- (18) Chen, L. X.; Zhang, X.; Shelby, M. L. Recent advances on ultrafast X-ray spectroscopy in the chemical sciences. *Chem. Sci.* **2014**, *5*, 4136–4152.
- (19) Attar, A. R.; Bhattacharjee, A.; Pemmaraju, C. D.; Schnorr, K.; Closser, K. D.; Prendergast, D.; Leone, S. R. Femtosecond x-ray spectroscopy of an electrocyclic ring-opening reaction. *Science* **2017**, *356*, 54–59.
- (20) Bhattacharjee, A.; Pemmaraju, C. D.; Schnorr, K.; Attar, A. R.; Leone, S. R. Ultrafast Intersystem Crossing in Acetylacetone via Femtosecond X-ray Transient Absorption at the Carbon K-Edge. *J. Am. Chem. Soc.* **2017**, *139*, 16576–16583, PMID: 29083165.

- (21) Neville, S. P.; Chergui, M.; Stolow, A.; Schuurman, M. S. Ultrafast X-Ray Spectroscopy of Conical Intersections. *Phys. Rev. Lett.* **2018**, *120*, 243001.
- (22) Yang, J. et al. Imaging CF₃I conical intersection and photodissociation dynamics with ultrafast electron diffraction. *Science* **2018**, *361*, 64–67.
- (23) Zinchenko, K. S.; Ardana-Lamas, F.; Seidu, I.; Neville, S. P.; Van Der Veen, J.; Lantfaloni, V. U.; Schuurman, M. S.; Wóner, H. J. Sub-7-femtosecond conical-intersection dynamics probed at the carbon K-edge. *Science* **2021**, *371*, 489.
- (24) Hua, W.; Mukamel, S.; Luo, Y. Transient X-ray Absorption Spectral Fingerprints of the S1 Dark State in Uracil. *J. Phys. Chem. Lett.* **2019**, *10*, 7172–7178.
- (25) Wolf, T. J. A. et al. Probing ultrafast $\pi\pi^*/n\pi^*$ internal conversion in organic chromophores via K-edge resonant absorption. *Nat. Commun.* **2017**, *8*, 29.
- (26) Nam, Y.; Keefer, D.; Nenov, A.; Conti, I.; Aleotti, F.; Segatta, F.; Lee, J. Y.; Garavelli, M.; Mukamel, S. Conical Intersection Passages of Molecules Probed by X-ray Diffraction and Stimulated Raman Spectroscopy. *J. Phys. Chem. Lett.* **0**, *0*, 12300–12309, PMID: 34931839.
- (27) CAMPBELL, J.; PAPP, T. WIDTHS OF THE ATOMIC K–N7 LEVELS. *At. Data Nucl. Data Tables* **2001**, *77*, 1–56.
- (28) Mukamel, S.; Rahav, S. In *Advances in Atomic, Molecular, and Optical Physics*; Arimondo, E., Berman, P., Lin, C., Eds.; Advances In Atomic, Molecular, and Optical Physics; Academic Press, 2010; Vol. 59; pp 223–263.
- (29) Finley, J.; Malmqvist, P.-Å.; Roos, B. O.; Serrano-Andrés, L. The multi-state CASPT2 method. *Chem. Phys. Lett.* **1998**, *288*, 299–306.
- (30) Forsberg, N.; Åke Malmqvist, P. Multiconfiguration perturbation theory with imaginary level shift. *Chem. Phys. Lett.* **1997**, *274*, 196–204.

- (31) Ghigo, G.; Roos, B. O.; Malmqvist, P.-Å. A modified definition of the zeroth-order Hamiltonian in multiconfigurational perturbation theory (CASPT2). *Chem. Phys. Lett.* **2004**, *396*, 142–149.
- (32) Widmark, P.-O.; Malmqvist, P.-Å.; Roos, B. O. Density matrix averaged atomic natural orbital (ANO) basis sets for correlated molecular wave functions. *Theor. Chim. Acta* **1990**, *77*, 291–306.
- (33) Malmqvist, P. Å.; Rendell, A.; Roos, B. O. The restricted active space self-consistent-field method, implemented with a split graph unitary group approach. *J. Phys. Chem.* **1990**, *94*, 5477–5482.
- (34) Delcey, M. G.; Sørensen, L. K.; Vacher, M.; Couto, R. C.; Lundberg, M. Efficient calculations of a large number of highly excited states for multiconfigurational wavefunctions. *J. Comput. Chem.* **2019**, *40*, 1789–1799.
- (35) Sauri, V.; Serrano-Andrés, L.; Shahi, A. R. M.; Gagliardi, L.; Vancoillie, S.; Pierloot, K. Multiconfigurational Second-Order Perturbation Theory Restricted Active Space (RASPT2) Method for Electronic Excited States: A Benchmark Study. *J. Chem. Theory Comput.* **2011**, *7*, 153–168, PMID: 26606229.
- (36) Almlöf, J.; Taylor, P. R. General contraction of Gaussian basis sets. I. Atomic natural orbitals for first- and second-row atoms. *J. Chem. Phys.* **1987**, *86*, 4070–4077.
- (37) Roos, B. O.; Lindh, R.; Malmqvist, P.-Å.; Veryazov, V.; Widmark, P.-O. New Relativistic ANO Basis Sets for Transition Metal Atoms. *J. Phys. Chem. A* **2005**, *109*, 6575–6579, PMID: 16834004.
- (38) Segatta, F.; Russo, M.; Nascimento, D. R.; Presti, D.; Rigodanza, F.; Nenov, A.; Bonvicini, A.; Arcioni, A.; Mukamel, S.; Maiuri, M.; Muccioli, L.; Govind, N.; Cerullo, G.; Garavelli, M. In *Silico Ultrafast Nonlinear Spectroscopy Meets Experiments: The Case*

- of Perylene Bisimide Dye. *J. Chem. Theory Comput.* **2021**, *17*, 7134–7145, PMID: 34676761.
- (39) Fdez. Galván, I. et al. OpenMolcas: From Source Code to Insight. *J. Chem. Theory Comput.* **2019**, *15*, 5925–5964.
- (40) Weingart, O.; Nenov, A.; Altoè, P.; Rivalta, I.; Segarra-Martí, J.; Dokukina, I.; Garavelli, M. COBRAMM 2.0 — A software interface for tailoring molecular electronic structure calculations and running nanoscale (QM/MM) simulations. *J. Mol. Model.* **2018**, *24*, 271.
- (41) Reiter, S.; Keefer, D.; de Vivie-Riedle, R. *Quantum Chemistry and Dynamics of Excited States*; John Wiley & Sons, Ltd, 2020; Chapter 11, pp 355–381.
- (42) Tal-Ezer, H.; Kosloff, R. An accurate and efficient scheme for propagating the time dependent Schrödinger equation. *J. Chem. Phys.* **1984**, *81*, 3967–3971.
- (43) Thallmair, S.; Roos, M. K.; de Vivie-Riedle, R. Design of specially adapted reactive coordinates to economically compute potential and kinetic energy operators including geometry relaxation. *J. Chem. Phys.* **2016**, *144*, 234104.
- (44) Butterworth, S. On the Theory of Filter Amplifiers. *Experimental Wireless and the Wireless Engineer* **1930**, *7*, 536–541.
- (45) Bhattacharjee, A.; Schnorr, K.; Oesterling, S.; Yang, Z.; Xue, T.; de Vivie-Riedle, R.; Leone, S. R. Photoinduced Heterocyclic Ring Opening of Furfural: Distinct Open-Chain Product Identification by Ultrafast X-ray Transient Absorption Spectroscopy. *J. Am. Chem. Soc.* **2018**, *140*, 12538–12544.

Graphical TOC Entry

